Solar Energy Materials & Solar Cells 282 (2025) 113325

Contents lists available at ScienceDirect

Solar Energy Materials and Solar Cells

journal homepage: www.elsevier.com/locate/solmat

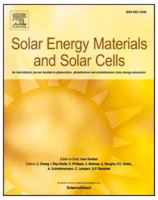

Unveiling the degradation mechanisms in silicon heterojunction solar cells under accelerated damp-heat testing

Xinyuan Wu [a,*], Xutao Wang [a], Ruirui Lv [b], Hao Song [b], Yuanjie Yu [b], Chandany Sen [a], Yuhao Cheng [a], Muhammad Umair Khan [a], Alison Ciesla [a], Tao Xu [b], Guangchun Zhang [b], Bram Hoex [a,**]

[a] *School of Photovoltaic and Renewable Energy Engineering, University of New South Wales, Sydney, Australia, 2052*
[b] *Canadian Solar Inc., Suzhou, Jiangsu, 215129, China*

ARTICLE INFO

Keywords:
Silicon heterojunction solar cells
Reliability
Contamination
Damp-heat stability

ABSTRACT

Silicon heterojunction (SHJ) solar cells have become one of the mainstream solar cells in the current photovoltaic market due to their high efficiency. Still, concerns about their long-term reliability are seen as a potential issue restricting further marketisation. In particular, the sensitivity of silicon heterojunction solar cells to high temperatures and moisture is a concern. Sodium (Na) in combination with humidity is widely considered one of the causes of degradation in silicon heterojunction solar cells. Yet, a comprehensive understanding of the mechanisms behind Na-induced decay remains lacking. This study will investigate humidity-induced degradation of industrial SHJ solar cells at elevated temperatures using various sodium-containing salts [sodium bicarbonate ($NaHCO_3$), sodium chloride (NaCl), and sodium nitrate ($NaNO_3$)] to improve our fundamental understanding of Na-induced degradation. We will show that SHJ solar cells exposed to $NaHCO_3$ and NaCl show a significant reduction in efficiency, while solar cells exposed to $NaNO_3$ show minimal degradation. Further analysis indicates that $NaHCO_3$ may interact with the transparent conductive oxide (TCO) layer, leading to a reduction in surface passivation and a deterioration of the metal-TCO interface. NaCl primarily affects the Ag contact, resulting in a reduction of the adhesion of the screen-printed contact. Moreover, the TCO composition, particularly the oxygen content, influences its chemical tolerance. These results show that Na-related degradation is more complicated than initially thought. The chemistry is strongly influenced by the negative ions, as well as the composition of TCO and metal paste. These factors are determined by the bill of materials and the contaminants introduced during cell/module fabrication and operation of the SHJ module. The findings of this paper may lead to the development of new accelerated testing protocols for SHJ technology to ascertain long-term reliability in the field.

1. Introduction

In the current era of growing demand for renewable energy sources, photovoltaics (PV) is gaining traction as a competitive option. Silicon-based solar modules presently dominate the global photovoltaic market due to their commendable cost-effectiveness [1]. Among emerging technologies, silicon heterojunction (SHJ) solar cells have attracted significant attention owing to their inherent advantages, such as simplified structure, low process temperatures during manufacturing, high open-circuit voltages, excellent temperature coefficients, and high bifaciality factors [2,3]. Substantial progress has been achieved in recent years in enhancing the efficiency of SHJ solar cells through dedicated research and technological advancements. Notably, LONGi has reached a remarkable milestone by pushing the efficiency record of such cells to 27.3 %, signalling a promising trajectory for this technology [4,5].

However, as SHJ technology gains wider application, reliability is emerging as a major concern compared to conventional c-Si solar cells [6]. Na is often identified as a primary contributor to the degradation of silicon solar devices [7–11]. Typically, industrial silicon modules utilise tempered soda-lime glass as the front and often also as the back sheet. This glass contains a significant amount of Na, which can migrate into solar cells through the encapsulant layers under field operation

---

[*] Corresponding author.
[**] Corresponding author.
E-mail addresses: xinyuan.wu@unsw.edu.au (X. Wu), b.hoex@unsw.edu.au (B. Hoex).

https://doi.org/10.1016/j.solmat.2024.113325
Received 31 October 2024; Accepted 24 November 2024

conditions. Na ions may interact with various anions from the environment and the module's bill of materials (BOM). Bicarbonate (HCO_3^-) may originate from tempered soda-lime glass as well, as sodium bicarbonate ($NaHCO_3$) is commonly added during glass fabrication to lower the melting point and enhance the chemical properties of the glass [12,13]. Moreover, sodium nitrate ($NaNO_3$) may serve as an additive in glass fabrication to reduce the melting point, enhance molten liquid flow, eliminate air bubbles and impurities, and improve glass transparency and quality [13–17]. Consequently, Na could potentially coexist with nitrate (NO_3^-) on the surface of solar cells over prolonged operational periods. Additionally, chloride (Cl^-) can be introduced by various environmental elements in the field, such as rainwater, soil, dust, and seawater, which may infiltrate and directly contact solar cells and water [18–21]. Studies by Segbefia et al. and Kumar et al. have demonstrated the presence of Na and Cl ions in the failed regions of solar modules installed outdoors for 20 years [10,22].

DH testing offers a swift means to simulate the degradation experienced over years of real-world use [23–25]. SHJ solar cells are notably vulnerable to such conditions, with the presence of Na-related impurities potentially worsening their degradation [9,10,26–29]. However, the chemical effects can vary depending on the specific ions involved [9,10,29]. Discrepancies emerged in experiments conducted at the cell level, revealing diverse impacts of Na-related impurities on SHJ cells. Adachi et al. and Li et al. utilised $NaHCO_3$ solution to expedite degradation and assess TCO stability [30–32]. Conversely, the use of NaCl led to notable increases in contact resistances due to degradation of metal contacts [21,33]. Nevertheless, a comprehensive examination of Na-related DH degradation has been lacking, emphasising the need for a deeper understanding and identification of degradation indicators at the cell level.

SHJ solar cells were found to undergo chemical deterioration in both metal contacts and TCO layers after 1000 to 3000 h of DH testing (equivalent to over 10 years of field operation) [31–35]. To expedite degradation testing further, cell-level testing has been suggested, typically involving the direct application of stressors onto the solar cells, followed by DH testing [21,28,31–34,36]. This approach enables swift evaluation of various cell technologies or processes and allows for a broader range of post-mortem analysis techniques to investigate the root causes of degradation.

Therefore, in this experiment, we conducted DH accelerated tests on SHJ solar cells and assessed the effects of three types of salt: $NaHCO_3$, NaCl, and $NaNO_3$. By tracking changes in electrical performance, we demonstrated the degradation caused by these Na-related salts and identified potential degradation regions in SHJ solar cells. Additionally, with the aid of advanced analysis techniques, we further investigated the structures and elements of TCO layers and metal contacts. We elucidated SHJ solar cell degradation under DH conditions caused by the combination of Na ions with different anions from a mechanistic perspective.

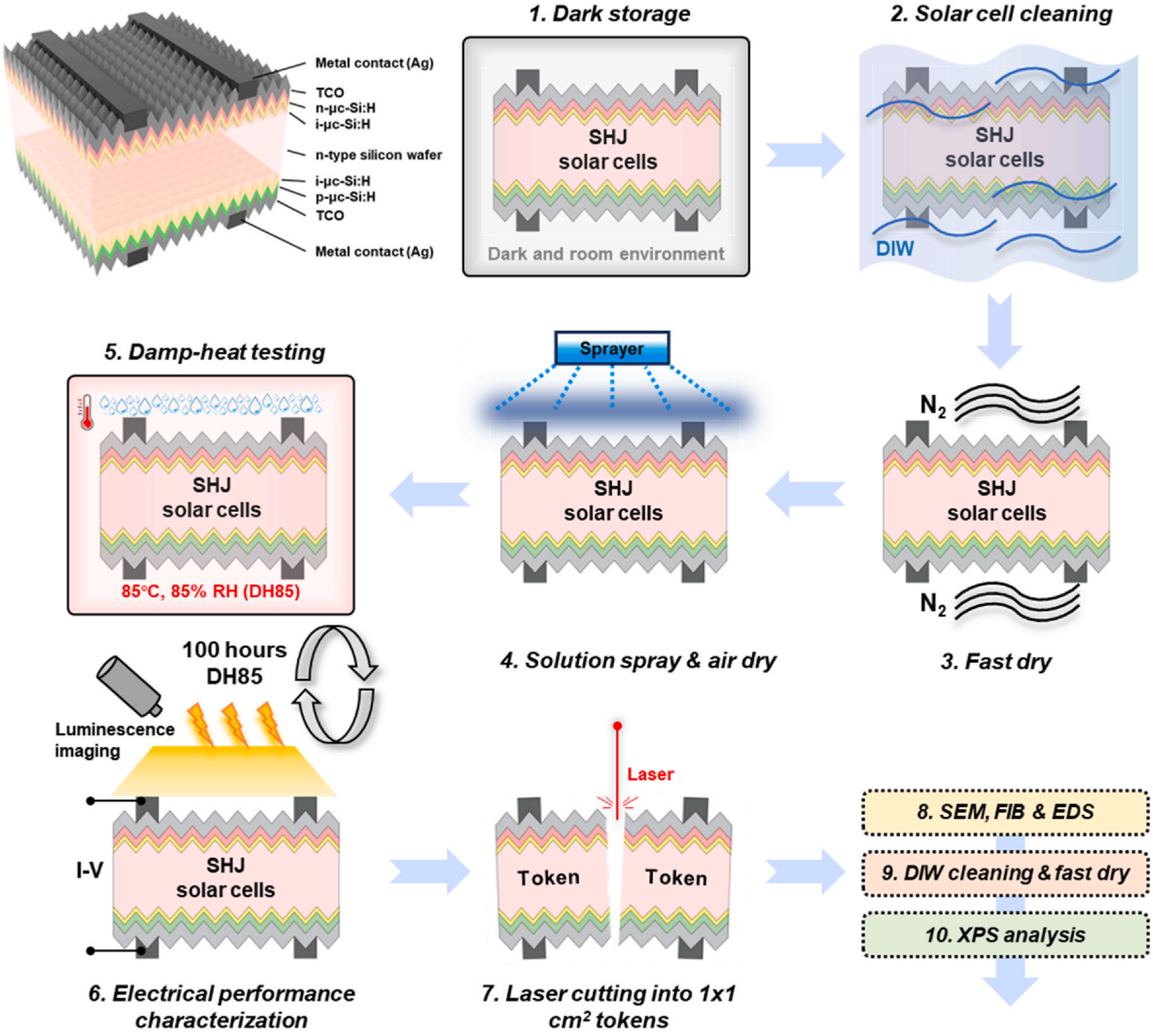

Fig. 1. Schematic of SHJ Solar cells and experimental flowchart for this work.

2. Experimental details

The samples utilised in the study comprised of M10 half-cut n-type industrial SHJ cells, measuring 182 mm by 91 mm with 10 busbars. The detailed schematic diagram for the SHJ cells used in this study is shown in Fig. 1. These SHJ cells featured intrinsic hydrogenated microcrystalline silicon (i-μc-Si:H) passivation layers on both surfaces, coupled with phosphorus-doped (n-μc-Si:H) and boron-doped (p-μc-Si:H) hydrogenated amorphous silicon layers on the front and rear sides, respectively. The front-side TCO consisted of indium oxide (InO), whereas the rear side was coated with an indium-doped tin oxide (ITO) layer. Each side featured a screen-printed H-pattern silver (Ag) grid. Before the experiment, all SHJ solar cells were stored in a dark, indoor environment with air exposure at room temperature to minimise any potential self-degradation during the experiment.

For the purposes of this research, $NaHCO_3$, NaCl and $NaNO_3$ were used as the Na-contaminants. The detailed experiment flow diagram is displayed in Fig. 1. Prior to conducting the experiments, all cells underwent a deionised water (DIW) cleaning, followed by a nitrogen gun drying to minimise potential contaminants. Subsequently, a 0.031 mol/L concentration of the designated salt solution was applied to the surface of each group's samples. Approximately 0.2 g of each solution was sprayed onto the surface of each cell, followed by a natural drying process inside a fume hood at ambient room temperature and atmospheric pressure. Throughout the application of the solutions, meticulous care was taken to handle the samples, ensuring the prevention of any contamination both within individual samples and across different samples. The DH test was carried out using an ASLi Environmental chamber, set to a temperature of 85 °C and a relative humidity of 85 % (DH85). Following each measurement interval, the climate chamber was allowed to cool to room temperature before being reheated for the following damp-heat testing cycle. Based on the sample treatment, all the cell samples were divided into seven groups: Control (without any treatment), $NaHCO_3$-front, $NaHCO_3$-rear, NaCl-front, NaCl-rear, $NaNO_3$-front and $NaNO_3$-rear.

The analysis of current-voltage (I-V) characteristics was conducted using a LOANA solar cell analysis system from pv-tools, with a tailored mask to fit the M10 half-cut cells and adjustments made to the contact frame to support the 10 busbars. The series resistance (R_s) values were measured by multi-light method [37]. A BTimaging R3 equipped with a high open-circuit voltage lens was employed to capture photoluminescence (PL) and R_s images, with subsequent image processing conducted via LumiTools software [38]. The transfer length method (TLM) was used to determine the sheet resistance (R_{sheet}) and contact resistivity (ρ_c) on c-Si(n)/i-μc-Si:H/(n)-μc-Si:H/ITO/metallisation samples which were specially prepared samples, using the pv-tools TLM-SCAN$^+$. Prior to the application of the solution, 6 mm strips were laser-cut from the SHJ cells' non-busbar regions using a FOBA M1000 scribing laser. The finger line resistance (R_{FL}) was measured by SEMIPROBE LA-150/LA-200 probe station.

Scanning electron microscopy (SEM) visuals were captured using a Zeiss 550 Crossbeam cryo-focused ion beam scanning electron microscope (cryo-FIB-SEM). The Oxford Instruments Ultim® Max detector facilitated energy-dispersive spectroscopy (EDS) analysis, which was interpreted with AZtec software. X-ray photoelectron spectroscopy (XPS) analyses were conducted to investigate the surface composition of the top 10 nm film on selected samples. Prior to XPS measurement, all samples were cleaned with DIW. The measurements were performed using a Thermo ESCALAB250Xi spectrometer equipped with a monochromatic Al K alpha X-ray source with an energy of 1486.68 eV and power of 120 W. The reference binding energy for analysing the C1s peak was set at 284.8 eV to account for any incidental hydrocarbon contamination.

3. Results and discussion

3.1. Electrical property variation

Prior to conducting the DH 85 tests, the SHJ solar cells from the experimental batch were assessed. The champion cell I-V information is shown in Fig. 2 (a), and the average power conversion efficiency (*PCE*) was found to be approximately 24.4 %, with an average open-circuit voltage (V_{oc}) of 746 mV, and the details are listed in Supplementary Table 1. The observed standard deviations for this set of cells indicate minimal variation. After the DH85 test, the SHJ solar cells exhibited varying degrees of degradation as shown in Fig. 2(b–f) and Supplementary Table 2. The Control group maintained a stable *PCE*, with negligible variations (~1.4%$_{rel}$) observed over the entire test duration, indicating that the SHJ solar cells were stable under the DH85 conditions. Conversely, the samples in Groups 2 and 3 (cells exposed to $NaHCO_3$) resulted in the most significant and rapid degradation. After a 20-h DH85 test, cells exposed to $NaHCO_3$ on the front side experienced a relative *PCE* reduction of ~80 %, with reductions of ~41%$_{rel}$ and ~12%$_{rel}$ in short-circuit current density (J_{sc}) and V_{oc}, respectively. The relative R_s increase reached ~2000 %, the highest among all experimental groups. Similarly, cells pre-treated with $NaHCO_3$ on the rear side exhibited a *PCE* reduction of approximately 41%$_{rel}$, primarily attributed to a V_{oc} drop of approximately 21%$_{rel}$. The relative R_s increase on cells pre-treated with $NaHCO_3$ on the rear side was limited to ~130%$_{rel}$. The degradation induced by $NaHCO_3$ occurred rapidly within the first 6 h, with V_{oc} and J_{sc} stabilising thereafter until the end of the testing period. NaCl exposure also led to cell degradation, consistent with our previous studies, albeit to a lesser extent due to a lower NaCl concentration used in this work [21,33]. The *PCE* reduction for cells with NaCl-treated front and rear sides after the 20-h DH85 test were ~10%$_{rel}$ and ~14%$_{rel}$, respectively, with V_{oc} losses mainly observed for the cell exposed at the rear (~1.2%$_{rel}$). While NaCl also contributed to an increase in R_s, the magnitudes were lower than those observed with $NaHCO_3$ at equivalent concentrations. In contrast, SHJ solar cells exposed to $NaNO_3$ were found to be relatively stable. After the 20-h DH85 test, the *PCE* reduced only ~2.5%$_{rel}$ and ~3.0%$_{rel}$ for the SHJ solar cells exposed to $NaNO_3$ at the front or rear, respectively. These losses could be attributed to a slight increase in R_s.

PL images were employed to assess the extent and uniformity of the recombination induced by the accelerated testing. As depicted in Fig. 3 (a), $NaHCO_3$ led to a rapid and uniform decrease in PL intensity. $NaHCO_3$ exposure on the front side resulted in a ~91%$_{rel}$ in PL counts, whereas this reduction was ~100%$_{rel}$ for $NaHCO_3$ exposure on the rear side. Notably, even though the SHJ solar cell exposed to $NaHCO_3$ on the front side showed the largest reduction after 1 h, it showed a lower relative reduction after 20 h compared to the sample exposed on the rear side, consistent with the relative changes observed in V_{oc} as shown in Fig. 3. In contrast, NaCl exposure on the front side did not significantly affect the PL intensity of the SHJ solar cells throughout the testing period, while NaCl exposure on the rear side resulted in a significant reduction in the PL intensity after 20 h of DH85 testing with a relative decrease of ~39 %. This was, however, significantly more severe than the SHJ solar cell exposed to $NaHCO_3$ on the rear side. Conversely, after DH85 testing, samples treated with $NaNO_3$ showed stable PL intensity similar to the control group, with variations of only ~2.8%$_{rel}$ and ~1.3%$_{rel}$ for $NaNO_3$ on the front and rear sides, respectively.

The trends in ΔR_s were comparable across Fig. 2 (f) and Fig. 3 (b), although minor disparities could arise from variations in contact configurations, measurement techniques, and tool limitations. Fig. 3 (b) demonstrates that both the control group and $NaNO_3$-treated groups exhibited no significant deterioration in R_s. However, the $NaHCO_3$-front sample displayed a rapid R_s surge to ~660 % relative after DH85 testing. Detectable R_s counts were limited to areas near busbars after the 20-h DH85 testing, likely due to spectral limitations and tool constraints. This discrepancy may contribute to the relative increase variations

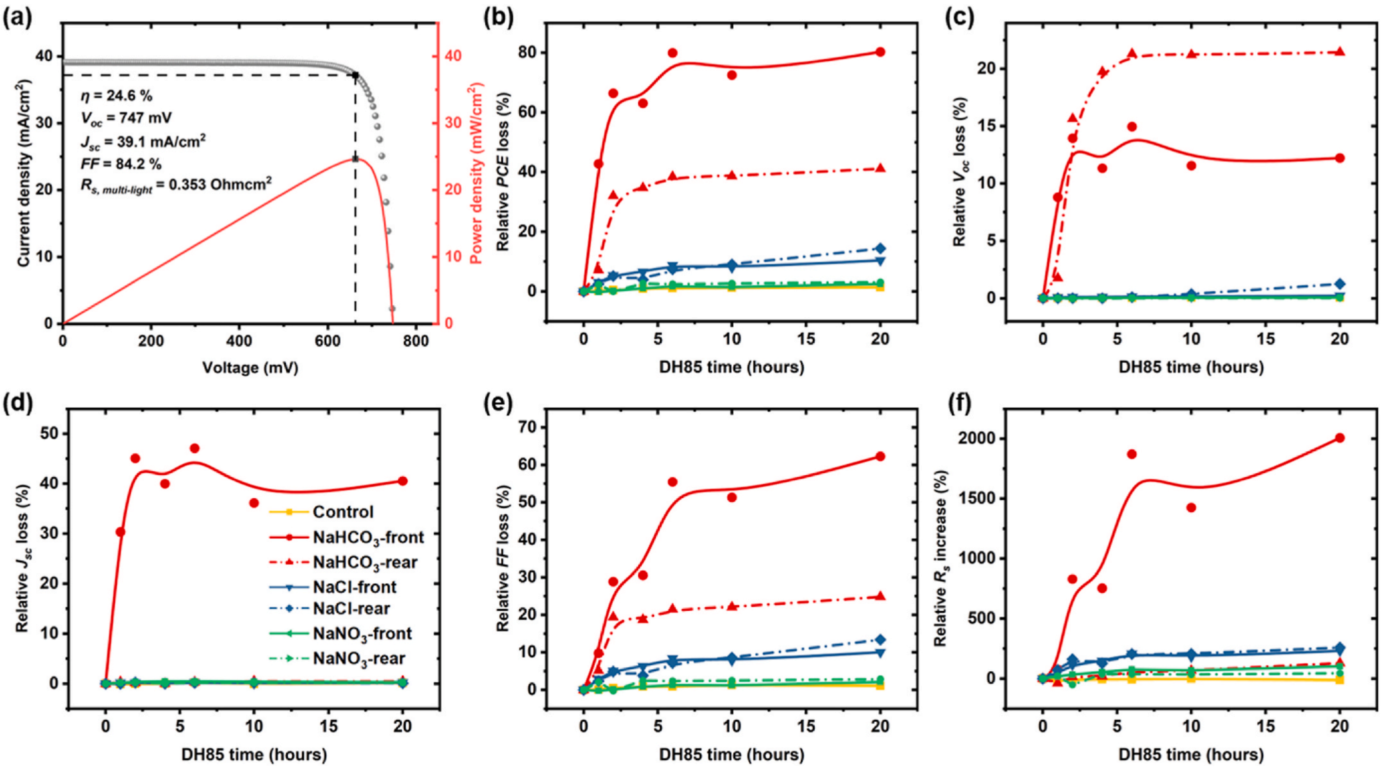

Fig. 2. (a) I-V curve of the champion SHJ cell from the experiment batch, and relative changes in (b) PCE, (c) J_{sc}, (d) V_{oc}, (e) FF, and (f) R_s as a function of DH85 duration for each group.

observed between Fig. 2 (f) and Fig. 3 (b). For the $NaHCO_3$-rear sample, the relative increase amplitude from R_s imaging was ~115 %, consistent with the R_s increase (~120%$_{rel}$) observed via I-V measurements. In comparison to the $NaHCO_3$-front, the R_s image of $NaHCO_3$-rear appeared more blurred after the 20-h DH85 test. This blurring could stem from the requirement in R_s imaging extraction to calculate the difference between two distinct PL images with current extraction under varying illumination conditions [39]. $NaHCO_3$ notably degraded the rear side contacts, leading to a diminished PL response (~99 % relative count decrease), thereby preventing sufficient count differentiation for tool processing.

In terms of the NaCl groups, NaCl-front exhibited a relative increase in R_s of ~41 %, while NaCl-rear showed a much higher relative increase of about 270 %. The greater rise in R_s observed in NaCl-rear compared to NaCl-front could be attributed to differences in finger size and quantity. There are more fingers present on the front side than on the rear side, and the aspect ratio of the fingers on the front side is larger than that on the rear side. These design choices aim to balance the optical and electrical characteristics of the cells and likely contribute to variations in degradation levels during the experimental period of DH85. Different from $NaHCO_3$ groups, NaCl rose R_s first at the early stage rather than recombination issues. It is hypothesised that $NaHCO_3$ degraded the surface layers first, and NaCl could play a role in the contact degradation.

To go deeper into the root causes of degradation, TLM was employed to measure the R_{sheet} and contact ρ_c of the front sides of cell stripes exposed to salt and subsequent DH85 testing for up to 2 h. As illustrated in Fig. 3 (c), the average R_{sheet} values remained relatively stable across all groups. However, a notable divergence in the R_{sheet} data was observed in the $NaHCO_3$ group, whereas the remaining groups exhibited a more consistent range of extracted R_{sheet} values. Notably, only the $NaHCO_3$ group displayed a significant increase in the ΔR_{sheet} standard deviation, indicating potential effects on the contact layers of SHJ solar cells after the testing period. Variations in ρ_c were observed in the $NaHCO_3$ and NaCl groups, while $NaNO_3$ samples maintained stable ρ_c ranges and values throughout the testing period. Specifically, the average measured ρ_c increased from ~4.3 to ~9.9 mΩ cm^2 for $NaHCO_3$ and from ~4.4 to ~11.5 mΩ cm^2 for NaCl after 2 h of DH85. Although the average increase from $NaHCO_3$ was not statistically significant compared to the NaCl group, as shown in Fig. 6 (b), we found a significantly large spread in values.

Furthermore, to assess metal contact properties, finger line resistances (R_{FL}) were measured from different groups after 20 h of DH85 testing, as shown in Fig. 3 (e) and Supplementary Fig. 1. The front-side line resistance values for all groups ranged from 2.1 to 2.4 Ω/cm, while the line resistance range for rear-side groups ranged from 3.1 to 3.3 Ω/cm. Minimal differences were observed between each group for both front-treated and rear-treated samples, with no obvious discrepancies in resistance with varying salt compositions. Considering the significant increase in R_s extracted from the *I-V* measurements, it can be concluded that this increase in R_s can be fully attributed to the changes in contact resistance between the TCO and the Ag metallisation.

3.2. Surface degradation analysis

SEM imaging coupled with EDS analysis was utilised to examine changes on the surface subsequent to DH85 testing. SEM images in Fig. 4 (a) show the samples' front surfaces following exposure to contaminants. The rear sides have a similar degradation trend, as plotted in Supplementary Information Figs. S2 and S3. Corresponding EDS spectra and elemental ratio analyses are presented in Fig. 4 (b) and Supplementary Table 3. Comparative analysis with control groups revealed similar appearances on both front and rear sides in SEM images. However, notable distinctions were observed in the elemental atomic ratio. There is no Sn signal on the front side, while the atomic ratio of In-to-Sn on the rear side was approximately 10:1, which is generally consistent with the process recipe design. Control samples displayed pristine surfaces devoid of contamination, with the Si signal predominantly

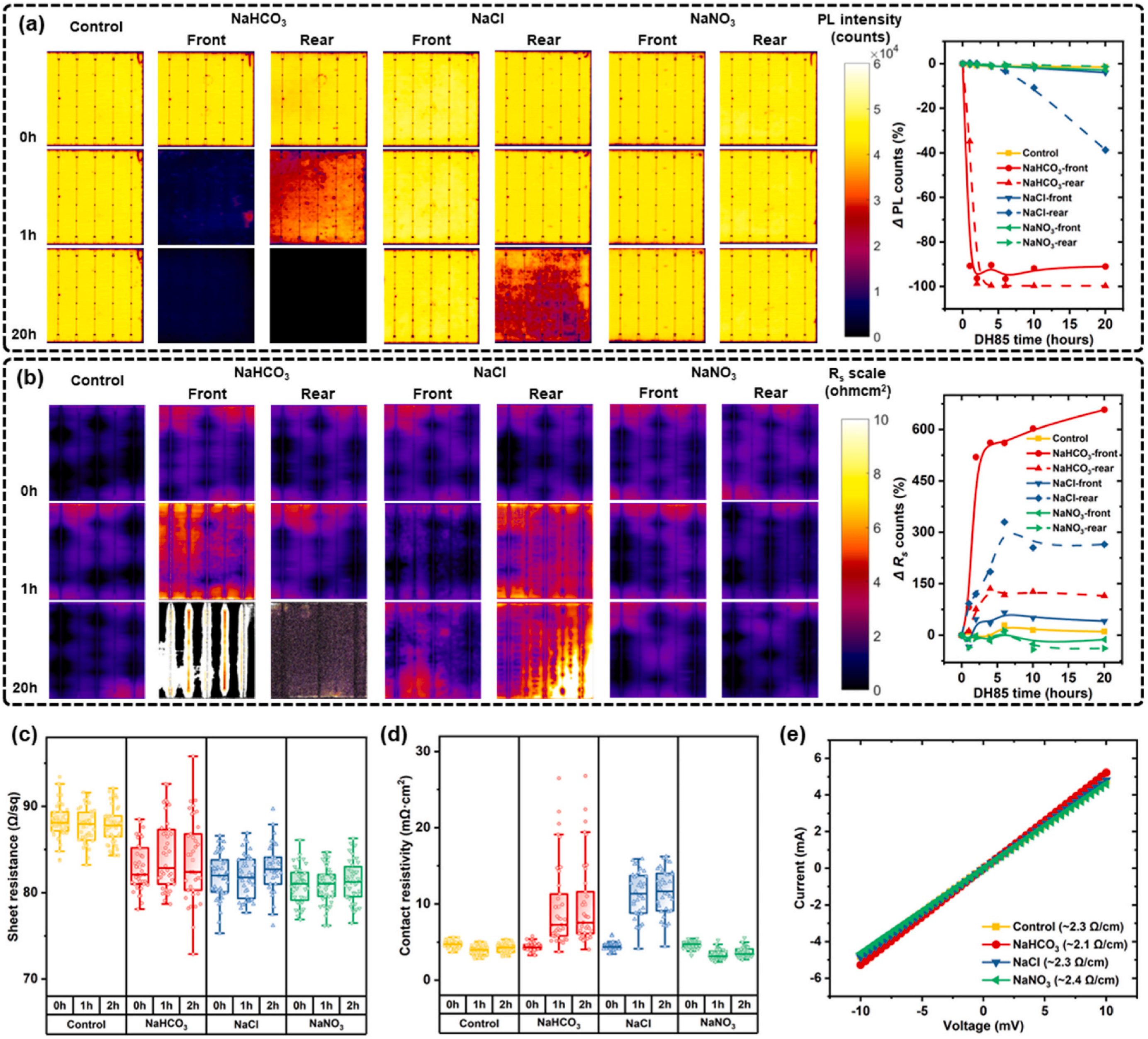

Fig. 3. (a) PL and (b) R_s images of SHJ solar cells from all groups before (0 h) and after 1 h and 20 h of the DH85 test and the relative count changes as a function of DH85 duration for all groups; The variations of (c) sheet resistance (R_{sheet}) and (d) contact resistivity (ρ_c) and (e) finger line resistance (R_{FL}) with DH85 time increase to 2 h of the front sides.

concentrated at the base of the pyramid. This non-uniform Si distribution might stem from the unevenness of the sputtering process on textured surfaces, potentially rendering certain Si layers more susceptible to contamination [40,41].

Even among samples exposed to contaminants, the front-side samples exhibited high consistency with the rear-side samples. For samples exposed to $NaHCO_3$, SEM imaging revealed random and non-uniform textures on the pyramid surface, with Si signal distributions differing from control groups. The distribution of the Si signal was no longer consistent with the control groups. Blurry, boundary-like bright regions indicated an increased detection of Si signals by EDS. Atomic ratio analysis in Fig. 4 (d) further confirmed higher Si counts in regions with elevated signal levels. Moreover, Na and C signal distributions correlated with bright Si regions, suggesting $NaHCO_3$ degradation affecting the TCO and silicon layer properties. Conversely, samples treated with NaCl and $NaNO_3$ displayed distinct Si signal distributions, maintaining similar Si to TCO metal ratios as control groups. The Na signal distributions were concentrated, likely residues from the solution after DH85 testing. Therefore, no significant degradation was observed with NaCl and $NaNO_3$, indicating less likelihood of TCO layer degradation with these contaminants.

Comparison between samples suggests $NaHCO_3$, due to its alkaline properties, could react with surface materials such as InO/ITO and μc-Si layers under DH85, potentially damaging surface layer structure and properties. This damage facilitated Na ion diffusion into silicon surfaces and bulk, increasing recombination centres and deteriorating surface passivation, leading to significant changes in V_{oc} and R_{sheet}. Additionally, $NaHCO_3$-induced degradation of front-side surface layers could impact optical properties, resulting in decreased J_{sc}. Conversely, NaCl and $NaNO_3$, being chemically neutral to InO/ITO, likely remained on cell surfaces as precipitated crystals without significant reactivity. The different crystal systems of NaCl and $NaNO_3$ residues on SHJ solar cells'

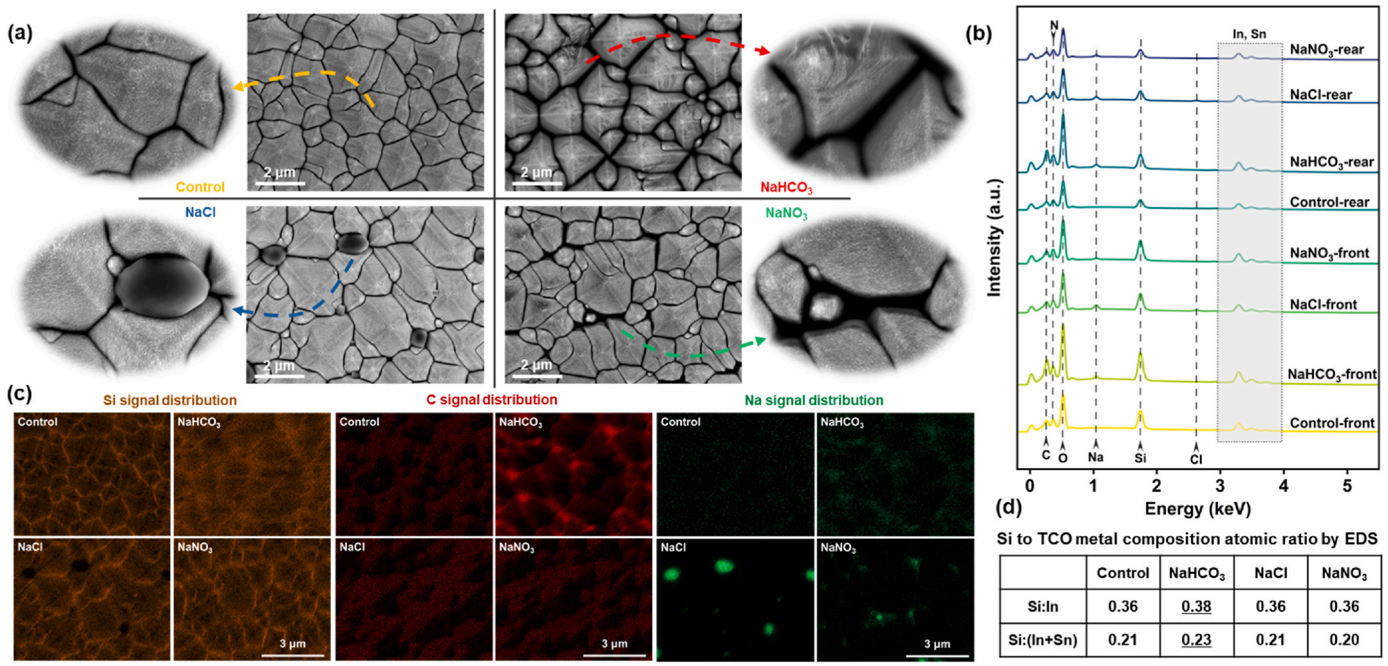

Si to TCO metal composition atomic ratio by EDS

	Control	NaHCO$_3$	NaCl	NaNO$_3$
Si:In	0.36	0.38	0.36	0.36
Si:(In+Sn)	0.21	0.23	0.21	0.20

Fig. 4. (a) Top-view SEM images of SHJ samples exposed to contaminants after 20 h of DH85, with corresponding EDS (b) spectrum and (c) mappings of Si, C, and Na, and (d) Si to TCO metal composition atomic ratio for each experiment group.

surfaces further differentiated their effects [42,43].

XPS analysis was utilised to further probe changes in surface layer properties, providing valuable insights into the failure mechanisms of InO/ITO coatings on both the front and rear sides of SHJ solar cells, as elaborated in Fig. 5. The control groups depicted in Fig. 5 (a) exhibit distinct O peaks at approximately 529.6, 531.2, and 532.0 eV, corresponding to lattice oxygen (O−In), oxygen-deficient (O-deficient), and hydroxyl groups (O−H), respectively [44–50]. O−In signifies oxygen

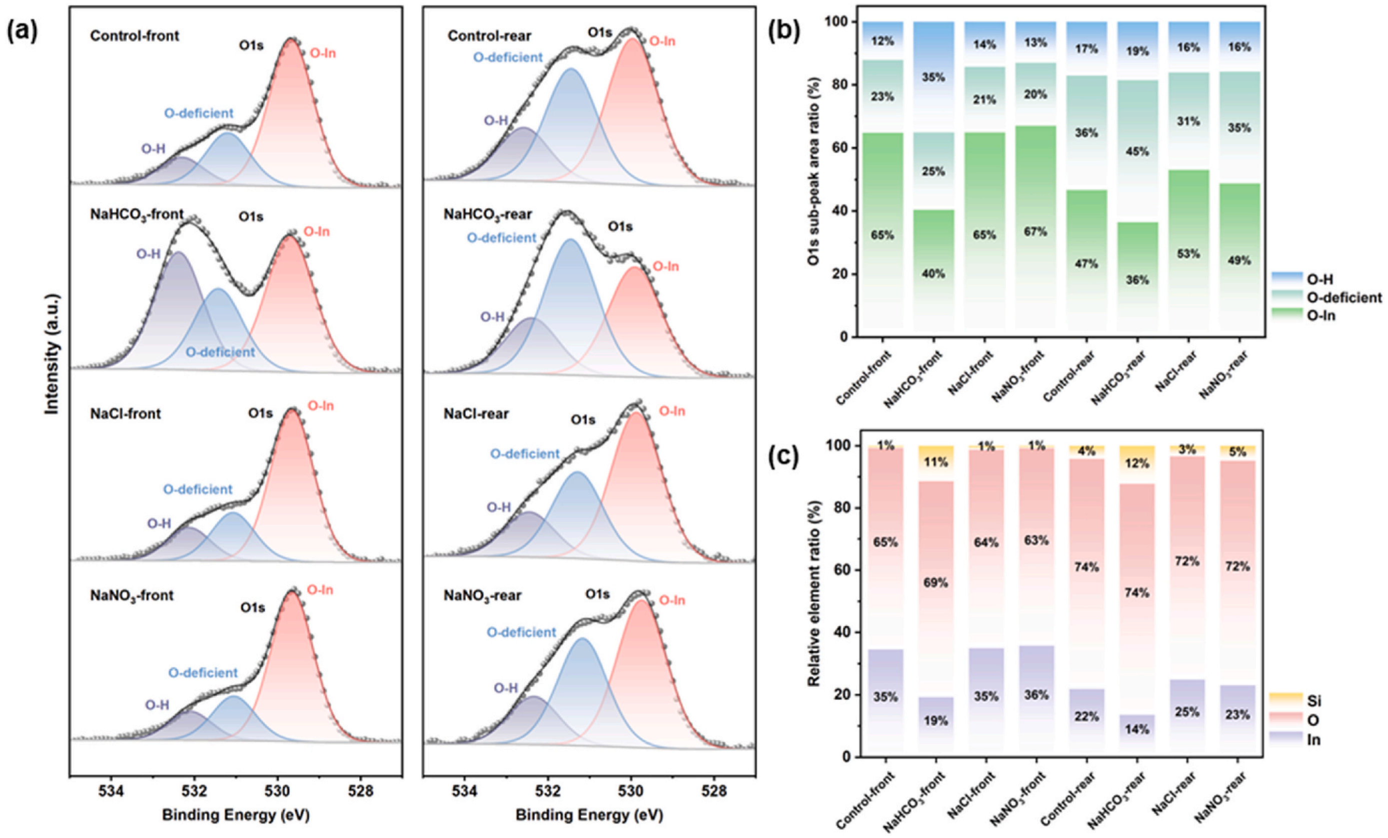

Fig. 5. (a) XPS O1s spectra of TCO layers (b) O1s sub-peak area ratio of lattice oxygen (O−In), oxygen-deficient (O-deficient) and hydroxyl groups (O–H), and (c) the relative Si, O and In atomic ratio of all experimental SHJ samples after 20 h of DH85 testing.

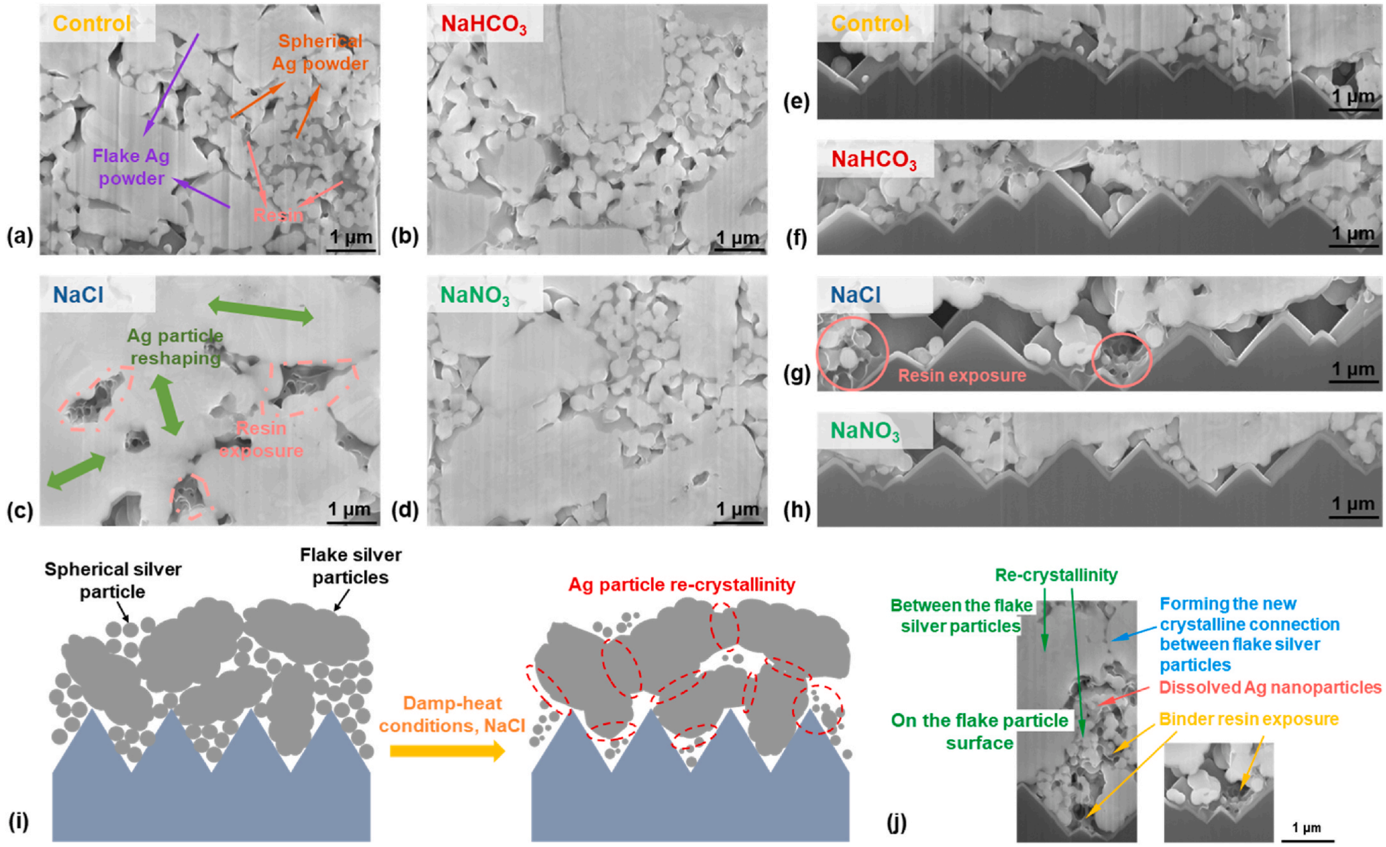

Fig. 6. Cross-section SEM images of the (a–d) Ag finger bulk, and (e–h) Ag/Si interface treated with $NaHCO_3$, NaCl, $NaNO_3$, and control group; (i) Proposed model for SHJ Ag contact failure caused by NaCl under damp-heat conditions; (j) Example of the failed Ag contact after NaCl-related damp-heat testing.

atoms positioned within the ITO lattice structure, which are crucial for maintaining crystalline integrity and a wide bandgap and ensuring high transparency in the visible spectrum. Conversely, O-deficient peaks indicate locations where oxygen atoms are absent from the lattice, serving as donors to the conduction band, thereby enhancing electrical conductivity. However, excessive oxygen vacancies can compromise transparency, as observed by a lower oxygen-deficient peak area ratio on the front side compared to the rear side in the control groups. Additionally, O−H, whether adsorbed on the surface or within lattice defects, may introduce localised states, potentially hindering carrier mobility and thereby reducing overall conductivity. Given the distinct optical and conductivity requirements of the front and rear sides, variations in oxygen oxidation state between the Control-front and Control-rear groups are apparent.

Upon comparison of Fig. 5(a) and (b), the sub-peaks corresponding to O in NaCl-front and the two $NaNO_3$ groups exhibited consistency with those observed in the corresponding Control groups. However, a distinct trend emerged with $NaHCO_3$ treatment after a 20-h exposure to DH85 conditions. In $NaHCO_3$-exposed samples, there was a notable increase in the O-deficient peak, while the O-In peak experienced a reduction, particularly pronounced in $NaHCO_3$-front samples. Specifically, the O-In peak in $NaHCO_3$-front samples constituted only ~40 % of the total O peak, representing a substantial decrease of ~25 % compared to Control-front samples. This suggests a potential breakdown of the O-In structure induced by $NaHCO_3$ under DH85 conditions. Moreover, the observed increase in the O-H ratio implies a higher likelihood of carrier trapping. However, despite these detrimental effects on the crystalline structure, the significant increase in O-deficient peaks could contribute to enhanced electrical conductivity. Consequently, while the average R_{sheet} values remain similar post-DH85 treatment with $NaHCO_3$, no aggregation was observed in Fig. 3(c) and (d). Similar trends were observed in $NaHCO_3$-rear samples, where the O-In peak underwent a noticeable increase (~11 %) while experiencing a decrease (~9 %) of O-deficient compared to Control-rear. This indicates structural damage to the ITO layer induced by $NaHCO_3$ treatment, leading to deteriorated electrical performance.

This observation suggests that the reaction between $NaHCO_3$ and the surface layers may cause localised removal of TCO layers and potential damage to the µc-Si layer, leading to deterioration of surface passivation. Additionally, increased exposure of Si to Na and other contaminants could further increase the recombination centre density. This damage might explain the observed variations in surface texture and the Si EDS signals in the $NaHCO_3$-treated samples, as shown in Fig. 4. Consequently, these changes can exacerbate recombination issues and result in a drop in V_{oc} [31,32,34].

While NaCl also resulted in increased recombination at the rear side, its impact was limited at the front side. Furthermore, the analysis of Fig. 5 (a) and (c) indicates that NaCl exposure did not significantly affect the relative ratios of Si, O, and In or the surface morphology. This discrepancy might be attributed to the presence of more O-deficient sites and a lower crystallinity of the rear-side ITO compared to the front side. As a result, a more oxygen-deficient structure could facilitate more Na transport through the TCO layer and further affect the µc-Si layer passivation properties as well as the silicon substrate surface recombination. Furthermore, the combined effects of NaCl and DH85 treatment resulted in a reduction in the O-deficient peak ratio, potentially due to Na ions occupying vacancy positions and forming O-Na bonds. The similar peak positions of O in metal oxides could lead to overlapping peaks, where O-Na bonds could overlap with O-In, contributing to a larger ratio of labelled O-In, possibly including O-Na [51–53]. However, this reaction could be limited to the ratio of O-deficient according to the O status comparison of the front and rear sides. This is likely to lead to differences in Na transfer, consequently resulting in the observed V_{oc} differences between NaCl-front and NaCl-rear samples.

In contrast, previous measurement results show no apparent recombination issues in SHJ solar cells exposed to $NaNO_3$. Considering that both NaCl and $NaNO_3$ could be seen as chemically neutral to TCO materials, this clearly demonstrates that anion should also be considered when explaining the cause of Na-related degradation. NO_3^- possesses a larger size compared to Cl^-, which is a monoatomic anion. As previously mentioned, O-deficient refers to vacancies formed by the detachment of O in the crystal lattice of metal oxides or other oxygen-containing compounds, resulting in an oxygen deficiency. This vacancy could easily allow the monatomic anions, like Cl^-, to transport. However, for $NaNO_3$, NO_3^- has a robust structure due to stable covalent bonds between oxygen and nitrogen. It is unlikely that NO_3^- will split into multiple monatomic ions, making it difficult for NO_3^- to diffuse through TCO layers under normal experimental conditions due to its size. Additionally, Na^+ and NO_3^- form extremely strong ionic bonds, so Na^+ could remain on the TCO surfaces to maintain electrical neutrality if NO_3^- does not diffuse in. Consequently, under our experimental conditions, it is less likely for Na^+ and NO_3^- to diffuse through vacancies within the ITO. Therefore, without Na diffusion, the sample exposed to $NaNO_3$ still performed well even after 20 h of DH85 testing.

3.3. *Contact failure analysis*

Normally, the low-temperature sintering Ag paste for industrial SHJ solar cell applications contains Ag powders, resin, additives, and solvents. For this work, the fingers were found to be a mixture of flake and spherical Ag powders. Flake Ag powder typically ranges in particle size from several micrometres to tens of micrometres, boasting a significant specific surface area for enhanced conductivity through increased contact area. With an average thickness of 50–150 nm, flake Ag powder exhibits exceptional conductivity and malleability. Its high purity and unique microstructure contribute to superior conductivity, reducing resistance and maximising efficiency. Additionally, flake Ag powder demonstrates excellent stability in conductive Ag paste, retaining its conductivity over extended periods without oxidation or degradation [54–58]. Spherical Ag powder possesses a uniform spherical configuration, featuring a high sphericity ratio that minimises variance between its average particle size and equivalent diameter. Despite its lower specific surface area, this structure boasts a higher particle density, facilitating the formation of a compact conductive layer and exceptional filling capability [59–61]. The resin, usually made of epoxy resin for industrial SHJ solar cell applications, acts as a binder in the Ag paste, holding the metallic particles together and adhering them to the TCO layer, ensuring strong adhesion [62–64]. Additives such as a coupling agent enhance resin adhesion, an anti-aging agent improves resin weather resistance, and a curing agent facilitates resin curing under heat exposure [65–67]. The paste's solvent typically consists of an environmentally friendly solvent with a high boiling point, utilised for viscosity adjustment and printing [68–70]. In the sintering process, the solvent evaporates, allowing the resin and additives to solidify and adhere to the Ag powder, forming the metal contacts. In this study, while the front-side and rear-side pastes share similar compositions, the primary distinctions lie in the height and size of the fingers. Specifically, the rear-side fingers exhibit a lower height and smaller size compared to those on the front side.

FIB-SEM was used to investigate the degradation of contacts in greater detail from finger bulk and finger/Si interfaces, as shown in Fig. 6(a–h), with the corresponding images and EDS mapping presented in Supplementary Information Figs. S6 and S7. As shown in Fig. 6 (a) and (e), the FIB-SEM images of the control groups also display two types of Ag particles tightly adhered by resin. As previously described, spherical Ag particles fill the gaps between flake Ag particles and the interfaces between the Ag contact and the silicon surface. Notably, no significant variations in the Ag structure were observed in samples from the $NaHCO_3$ and $NaNO_3$ groups. Additionally, the C atomic ratios of the NaCl samples did not change significantly, and it has been shown that epoxy resin can tolerate Na salt environments and resist metal corrosion [71–74].

Attention is directed towards the samples treated with NaCl. In Fig. 6 (c), some flake Ag particles were observed to bind together, while the size of the spherical Ag particles and their corresponding fill effect were reduced. Consequently, as shown in Fig. 6 (g), the degradation of spherical Ag particles resulted in more voids between the metal contact and the TCO layer, potentially with mesh binding resin observed at the interface region. Limited spherical Ag particles could be observed in the metal bulk and the interface. Despite this, the metal conductivity of the new Ag finger structure remained consistent with the control group, as indicated by the R_{FL} values presented in Fig. 3 (e). This suggests that the NaCl treatment did not materially affect the effective Ag content of the metal contact. However, the effective contact area between Ag and ITO in the NaCl-treated samples was reduced compared to the rest groups due to the increase in void size. This reduction in contact area likely accounts for the significant rise in R_s observed in the NaCl-treated samples. The examination of samples exposed to NaCl revealed a distinct metal degradation mechanism. Research indicates that Ag nanoparticles are likely to dissolve in a NaCl environment due to their active properties [75–81]. Studies by Yang et al. and Wiley et al. demonstrate that Ag nanoparticles can also undergo a recrystallisation process into larger Ag particles, primarily due to the effects of chloride ions (Cl^-) [82,83]. According to their findings, the etching of Ag nanoparticles by dissolved O_2 and Cl^- was first proposed by Wiley et al. [83]. They confirmed that chloride ions, rather than alkali metal cations, induce the oxidative dissolution of Ag nanoparticles by substituting NaCl with KCl while maintaining other experimental conditions constant. Henglein et al. noted that adding a coordinating anionic ligand to an Ag sol accelerates the oxidative dissolution of Ag [84]. They suggested that for an Ag atom on the particle's surface to bind with a ligand, it must transfer some negative charge to other surface Ag atoms. This increased electronegativity makes neighbouring atoms more susceptible to oxidation. The Ag ions released by the O_2/Cl^- etching of Ag nanoparticles are re-reduced in the reaction environment. Over time, the dynamics of the dissolution and regeneration of Ag particles and ions reach equilibrium, as shown in Eq. (1). Shown as Supplementary Fig. 12, Fargašová et al. provided evidence of NaCl treatment impact on Ag nanoparticles, which were recrystallised and clustered under different NaCl environments [85].

$$Ag + Cl^- \leftrightarrow AgCl + e^- (Eq.\ 1)$$

Based on this information from the literature, a possible model for SHJ Ag contact degradation under damp-heat conditions is proposed, as shown in Fig. 6 (i). Before NaCl damp-heat testing, nano-scale spherical Ag particles fill the gaps between flake Ag particles and the interface between the Ag and TCO layers. However, after damp-heat testing of NaCl-exposed samples, these nano-scale spherical Ag particles may dissolve and recrystallise on the crystalline flake Ag particles. Damp-heat treatment further encourages the recrystallisation of additional nano Ag-particles, increasing the size of the flake Ag particles. As a result, some flake Ag particles may connect, but more voids will form within the metal contacts and interface. Thus, the bulk conductivity of the Ag contact was not significantly affected by damp-heat NaCl exposure, as indicated by the R_{FL} values in Fig. 3 (e). The removal of Ag nanoparticles could expose the binder resin structure, as shown in Fig. 6 (g). The recrystallisation of Ag content could alter the original structural stress of the resin-bonded Ag particles. In more severe conditions, the resin structure might fracture at specific points due to its elasticity, worsening the adhesion of the Ag contact and the metal-Si interface. Consequently, the physical structure change between the metal and Si increases contact resistance due to less effective contact, which was also found in the work reported by Sen et al. [21].

In addition, R_s and ρ_c increases were observed in $NaHCO_3$ groups.

Unlike NaCl, $NaHCO_3$ primarily induced recombination issues, which subsequently led to contact failures from electrical property characterisation as shown in Fig. 3. Combining with previous EDS and XPS analysis, it was found that surface contact layers, such as TCO and μc-Si layers, could undergo significant deterioration after exposure to $NaHCO_3$ in DH85 testing conditions. Therefore, it is probable that the contact failure originated from the degradation of the contact layers rather than the Ag component.

4. Conclusion

In this study, we investigated the effects of three types of sodium-related salts ($NaHCO_3$, NaCl, and $NaNO_3$) on the damp-heat degradation of industrial SHJ solar cells. Our experimental results revealed that $NaHCO_3$ and NaCl caused significant reductions in relative efficiency, ranging from approximately 10 %–80 %, for both sides of the SHJ solar cells after 20 h of DH85. Specifically, $NaHCO_3$ treatment induced a rapid drop in V_{oc} and an increase in R_s, while NaCl primarily contributed to R_s increases and recombination issues at the rear sides of the cells. Conversely, $NaNO_3$ had minimal degradation, with efficiency reductions of only approximately 2 %–3 %, and the electrical parameters remained relatively stable during the test period.

In light of the previous analysis, it becomes evident that various Na salts possess the capability to initiate different degradation pathways involving distinct anionic species. $NaHCO_3$, characterised by its status as a strong base weak acid salt, engenders chemical reactions upon interaction with InO/ITO and μc-Si layers, thereby increasing surface recombination. The resultant contact failure may be attributed to the deleterious effects of this reaction on the interface between Ag and Si. Conversely, the degradation induced by NaCl primarily manifests within the metal, leading to the reshaping of Ag particles and the occurrence of delamination between Ag and ITO interfaces. Furthermore, NaCl may exacerbate recombination issues in instances where the InO/ITO layers are inadequately designed to mitigate oxygen vacancies. In contrast, $NaNO_3$ was found to be inert in terms of inducing degradation, suggesting that sodium-related degradation is triggered only under specific conditions. These findings underscore the intricate interplay between Na salts and their consequential impact on material degradation pathways, thereby highlighting the necessity for tailored design strategies to mitigate adverse effects in relevant applications.

In summary, this testing approach amplifies potential issues that may emerge in SHJ modules under operational conditions, enabling detailed characterization and precise identification of degradation pathways. This research highlights the significant influence of ion combinations on SHJ contact degradation mechanisms, providing valuable insights into the degradation patterns and influencing factors for TCO and metal contacts in SHJ solar cells. These findings support the evaluation of module-level reliability and underscore the need for optimized accelerated testing methods. Ultimately, this work advocates for process optimization to enhance the long-term reliability of SHJ solar cells and modules in practical applications.

CRediT authorship contribution statement

Xinyuan Wu: Conceptualization, Formal analysis, Investigation, Methodology, Validation, Visualization, Writing – original draft, Writing – review & editing. **Xutao Wang:** Formal analysis, Investigation, Methodology. **Ruirui Lv:** Formal analysis, Investigation, Methodology. **Hao Song:** Formal analysis, Investigation. **Yuanjie Yu:** Formal analysis, Investigation, Project administration. **Chandany Sen:** Data curation, Investigation, Methodology. **Yuhao Cheng:** Data curation, Investigation, Methodology. **Muhammad Umair Khan:** Investigation, Methodology. **Alison Ciesla:** Investigation, Methodology, Writing – review & editing. **Tao Xu:** Project administration, Resources. **Guangchun Zhang:** Funding acquisition, Project administration, Resources. **Bram Hoex:** Data curation, Formal analysis, Funding acquisition, Project administration, Resources, Supervision, Visualization, Writing – review & editing.

Declaration of competing interest

The authors declare the following financial interests/personal relationships which may be considered as potential competing interests: Bram Hoex reports financial support was provided by Australian Renewable Energy Agency. Bram Hoex reports financial support was provided by University of New South Wales. If there are other authors, they declare that they have no known competing financial interests or personal relationships that could have appeared to influence the work reported in this paper.

Acknowledgements

This work received support from the Australian Government through the Australian Renewable Energy Agency (ARENA 1–060 Extension project) and the Australian Centre for Advanced Photovoltaics (ACAP). The authors appreciate the support provided by the Australian Government's Trailblazer for Recycling & Clean Energy program, led by UNSW & the University of Newcastle. However, the Australian Government does not accept responsibility for the views, information, or advice expressed in this research. The authors would like to acknowledge the Electron Microscope Unit at The University of New South Wales (UNSW), specifically Dr Charlie Kong, Dr Yin Yao and Dr Karen Privat for their scientific and technical assistance and access to the facilities of the Australian Microscopy & Microanalysis Research Facility. The authors acknowledge the surface analysis laboratory, Solid State & Elemental Analysis Unit (SSEAU), Mark Wainwright Analytical Centre (MWAC), and UNSW for the support of XPS analysis. The authors also express their gratitude for the support provided by the entire team at the Solar Industrial Research Facility (SIRF) at UNSW.

Appendix A. Supplementary data

Supplementary data to this article can be found online at https://doi.org/10.1016/j.solmat.2024.113325.

Data availability

Data will be made available on request.

References

[1] M. Trommsdorff, I.S. Dhal, Ö.E. Özdemir, D. Ketzer, N. Weinberger, C. Rösch, Chapter 5 - agrivoltaics: solar power generation and food production, in: S. Gorjian, P.E. Campana (Eds.), Solar Energy Advancements in Agriculture and Food Production Systems, Academic Press, 2022, pp. 159–210.

[2] A. Razzaq, T.G. Allen, W. Liu, Z. Liu, S. De Wolf, Silicon heterojunction solar cells: techno-economic assessment and opportunities, Joule 6 (3) (2022/03/16/2022) 514–542, https://doi.org/10.1016/j.joule.2022.02.009.

[3] S. De Wolf, A. Descoeudres, Z.C. Holman, C. Ballif, High-efficiency silicon heterojunction solar cells: a review, green 2 (1) (2012) 7–24.

[4] H. Wu, et al., Silicon heterojunction back contact solar cells by laser patterning, Nature (2024/10/01 2024), https://doi.org/10.1038/s41586-024-08110-8.

[5] M.A. Green, et al., Solar cell efficiency tables (Version 64), Prog. Photovoltaics Res. Appl. 32 (7) (2024-07-01 2024) 425–441, https://doi.org/10.1002/pip.3831.

[6] O. Arriaga Arruti, A. Virtuani, C. Ballif, Long-term performance and reliability of silicon heterojunction solar modules, Prog. Photovoltaics Res. Appl. (2023-03-02 2023), https://doi.org/10.1002/pip.3688.

[7] W. Luo, et al., Potential-induced degradation in photovoltaic modules: a critical review, Energy Environ. Sci. 10 (1) (2017-01-01 2017) 43–68, https://doi.org/10.1039/c6ee02271e.

[8] S. Yamaguchi, C. Yamamoto, K. Ohdaira, A. Masuda, Comprehensive study of potential-induced degradation in silicon heterojunction photovoltaic cell modules, Prog. Photovoltaics Res. Appl. 26 (9) (2018-09-01 2018) 697–708, https://doi.org/10.1002/pip.3006.

[9] O.K. Segbefia, N. Akhtar, T.O. Sætre, Moisture induced degradation in field-aged multicrystalline silicon photovoltaic modules, Sol. Energy Mater. Sol. Cell. 258 (2023/08/15/2023) 112407, https://doi.org/10.1016/j.solmat.2023.112407.

[10] O.K. Segbefia, A.G. Imenes, T.O. Sætre, Moisture ingress in photovoltaic modules: a review, Sol. Energy 224 (2021/08/01/2021) 889–906, https://doi.org/10.1016/j.solener.2021.06.055.

[11] D. Lausch, et al., Sodium outdiffusion from stacking faults as root cause for the recovery process of potential-induced degradation (PID), Energy Proc. 55 (2014) 486–493.

[12] W. Lanford, K. Davis, P. Lamarche, T. Laursen, R. Groleau, R. Doremus, Hydration of soda-lime glass, J. Non-Cryst. Solids 33 (2) (1979) 249–266.

[13] R. Gy, Ion exchange for glass strengthening, Mater. Sci. Eng., B 149 (2) (2008/03/25/2008) 159–165, https://doi.org/10.1016/j.mseb.2007.11.029.

[14] S. Berneschi, G.C. Righini, S. Pelli, Towards a glass new world: the role of ion-exchange in modern technology, Appl. Sci. 11 (10) (2021) 4610.

[15] T. Izawa, H. Nakagome, Optical waveguide formed by electrically induced migration of ions in glass plates, Appl. Phys. Lett. 21 (12) (1972) 584–586.

[16] G. Stewart, P. Laybourn, Fabrication of ion-exchanged optical waveguides from dilute silver nitrate melts, IEEE J. Quant. Electron. 14 (12) (1978) 930–934.

[17] J.L. Jackel, Glass waveguides made using low melting point nitrate mixtures, Appl. Opt. 27 (3) (1988) 472–475.

[18] Z. Sharp, D. Draper, The chlorine abundance of Earth: implications for a habitable planet, Earth Planet Sci. Lett. 369 (2013) 71–77.

[19] T.E. Graedel, W. Keene, The budget and cycle of Earth's natural chlorine, Pure Appl. Chem. 68 (9) (1996) 1689–1697.

[20] A.J. Magenheim, A.J. Spivack, P.J. Michael, J.M. Gieskes, Chlorine stable isotope composition of the oceanic crust: implications for Earth's distribution of chlorine, Earth Planet Sci. Lett. 131 (3–4) (1995) 427–432.

[21] C. Sen, et al., Accelerated damp-heat testing at the cell-level of bifacial silicon HJT, PERC and TOPCon solar cells using sodium chloride, Sol. Energy Mater. Sol. Cell. 262 (2023/10/15/2023) 112554, https://doi.org/10.1016/j.solmat.2023.112554.

[22] S. Kumar, R. Meena, R. Gupta, Imaging and micro-structural characterization of moisture induced degradation in crystalline silicon photovoltaic modules, Sol. Energy 194 (2019/12/01/2019) 903–912, https://doi.org/10.1016/j.solener.2019.11.037.

[23] M. Koehl, S. Hoffmann, S. Wiesmeier, Evaluation of damp-heat testing of photovoltaic modules, Prog. Photovoltaics Res. Appl. 25 (2) (2017) 175–183.

[24] J. Zhu, et al., Changes of solar cell parameters during damp-heat exposure, Prog. Photovoltaics Res. Appl. 24 (10) (2016) 1346–1358.

[25] C. Peike, et al., Origin of damp-heat induced cell degradation, Sol. Energy Mater. Sol. Cell. 116 (2013) 49–54.

[26] J. Park, S.H. Park, S.-H. Jeong, J.-Y. Lee, J.Y. Song, Corrosion behavior of silver-coated conductive yarn, Front. Chem. 11 (2023).

[27] C. Sen, et al., Four failure modes in silicon heterojunction glass-backsheet modules, Sol. Energy Mater. Sol. Cell. 257 (2023/08/01/2023) 112358, https://doi.org/10.1016/j.solmat.2023.112358.

[28] L. Gnocchi, O.A. Arruti, C. Ballif, A. Virtuani, A comprehensive physical model for the sensitivity of silicon heterojunction photovoltaic modules to water ingress, Cell Reports Physical Science 5 (1) (2024).

[29] Q. Bai, H. Yang, C. Nan, H. Wang, Z. Chen, Analysis of the electrochemical reactions and ions migration for crystalline silicon solar module under high system voltage, Sol. Energy 225 (2021/09/01/2021) 718–725, https://doi.org/10.1016/j.solener.2021.07.050.

[30] H. Hiroi, Y. Iwata, S. Adachi, H. Sugimoto, A. Yamada, New world-record efficiency for pure-sulfide Cu (In, Ga) S 2 thin-Film solar cell with Cd-free buffer layer via KCN-free process, IEEE J. Photovoltaics 6 (3) (2016) 760–763.

[31] X. Li, et al., Potential-free sodium-induced degradation of silicon heterojunction solar cells, Prog. Photovoltaics Res. Appl. (2023), https://doi.org/10.1002/pip.3698.

[32] X. Li, et al., Highly crystallized tungsten doped indium oxide film stabilizes silicon heterojunction solar cells in sodium environment, Sol. Energy Mater. Sol. Cell. 233 (2021/12/01/2021) 111387, https://doi.org/10.1016/j.solmat.2021.111387.

[33] X. Wu, et al., Addressing sodium ion-related degradation in SHJ cells by the application of nano-scale barrier layers, Sol. Energy Mater. Sol. Cell. 264 (2024/01/01/2024) 112604, https://doi.org/10.1016/j.solmat.2023.112604.

[34] D. Adachi, T. Terashita, T. Uto, J.L. Hernández, K. Yamamoto, Effects of SiOx barrier layer prepared by plasma-enhanced chemical vapor deposition on improvement of long-term reliability and production cost for Cu-plated amorphous Si/crystalline Si heterojunction solar cells, Sol. Energy Mater. Sol. Cell. 163 (2017/04/01/2017) 204–209, https://doi.org/10.1016/j.solmat.2016.12.029.

[35] J. Karas, et al., Damp heat induced degradation of silicon heterojunction solar cells with Cu-plated contacts, IEEE J. Photovoltaics 10 (1) (2019) 153–158.

[36] P.M. Sommeling, J. Liu, J.M. Kroon, Corrosion effects in bifacial crystalline silicon PV modules; interactions between metallization and encapsulation, Sol. Energy Mater. Sol. Cell. 256 (2023/07/01/2023) 112321, https://doi.org/10.1016/j.solmat.2023.112321.

[37] K.C. Fong, K.R. McIntosh, A.W. Blakers, Accurate series resistance measurement of solar cells, Prog. Photovoltaics Res. Appl. 21 (4) (2013/06/01 2013) 490–499, https://doi.org/10.1002/pip.1216.

[38] D.N.R. Payne, C. Vargas, Z. Hameiri, S.R. Wenham, D.M. Bagnall, An advanced software suite for the processing and analysis of silicon luminescence images, Comput. Phys. Commun. 215 (2017/06/01/2017) 223–234, https://doi.org/10.1016/j.cpc.2017.02.012.

[39] H. Kampwerth, T. Trupke, J. Weber, Y. Augarten, Advanced luminescence based effective series resistance imaging of silicon solar cells, Appl. Phys. Lett. 93 (20) (2008) 202102.

[40] U. Barajas-Valdes, O.M. Suárez, Morphological and structural characterization of magnetron-sputtered aluminum and aluminum-boron thin films, Crystals 11 (5) (2021-04-28 2021) 492, https://doi.org/10.3390/cryst11050492.

[41] K. Shimizu, H. Habazaki, P. Skeldon, G. Thompson, G. Wood, Non-uniform sputtering and degradation of depth resolution during GDOES depth profiling analysis of thin anodic alumina films grown over rough substrates, Surf. Interface Anal.: An International Journal devoted to the development and application of techniques for the analysis of surfaces, interfaces and thin films 27 (10) (1999) 950–954.

[42] C. Bian, H. Chen, X. Song, J. Yu, Effects of organic pollutants on the fractional crystallization of NaNO3 from high-saline wastewater, J. Cryst. Growth 540 (2020/06/15/2020) 125656, https://doi.org/10.1016/j.jcrysgro.2020.125656.

[43] L.Z. Khadeeva, S.V. Dmitriev, Discrete breathers in crystals with NaCl structure, Phys. Rev. B 81 (21) (2010) 214306.

[44] J. Sheng, J. Park, D.-w. Choi, J. Lim, J.-S. Park, A study on the electrical properties of atomic layer deposition grown InO x on flexible substrates with respect to N2O plasma treatment and the associated thin-film transistor behavior under repetitive mechanical stress, ACS Appl. Mater. Interfaces 8 (45) (2016) 31136–31143.

[45] C. Donley, et al., Characterization of Indium−Tin oxide interfaces using X-ray photoelectron spectroscopy and redox processes of a chemisorbed probe molecule: effect of surface pretreatment conditions, Langmuir 18 (2) (2002-01-01 2002) 450–457, https://doi.org/10.1021/la011101t.

[46] G. Jung, et al., Transducer-aware hydroxy-rich-surface indium oxide gas sensor for low-power and high-sensitivity NO2 gas sensing, ACS Appl. Mater. Interfaces 15 (18) (2023/05/10 2023) 22651–22661, https://doi.org/10.1021/acsami.3c00022.

[47] Z.M. Detweiler, S.M. Wulfsberg, M.G. Frith, A.B. Bocarsly, S.L. Bernasek, The oxidation and surface speciation of indium and indium oxides exposed to atmospheric oxidants, Surf. Sci. 648 (2016/06/01/2016) 188–195, https://doi.org/10.1016/j.susc.2015.10.026.

[48] A. Chen, K. Zhu, H. Zhong, Q. Shao, G. Ge, A new investigation of oxygen flow influence on ITO thin films by magnetron sputtering, Sol. Energy Mater. Sol. Cell. 120 (2014) 157–162.

[49] S. Li, X. Qiao, J. Chen, Effects of oxygen flow on the properties of indium tin oxide films, Mater. Chem. Phys. 98 (1) (2006) 144–147.

[50] J. Kim, et al., X-ray photoelectron spectroscopy of surface-treated indium-tin oxide thin films, Chem. Phys. Lett. 315 (5–6) (1999) 307–312.

[51] S. Wu, Y. Qiao, K. Jiang, Y. He, S. Guo, H. Zhou, Tailoring sodium anodes for stable sodium–oxygen batteries, Adv. Funct. Mater. 28 (13) (2018) 1706374.

[52] B. Mao, et al., Operando ambient pressure X-ray photoelectron spectroscopy studies of sodium–oxygen redox reactions, Top. Catal. 61 (2018) 2123–2128.

[53] R. Manikandan, C.J. Raj, M. Rajesh, B.C. Kim, J.Y. Sim, K.H. Yu, Electrochemical behaviour of lithium, sodium and potassium ion electrolytes in a Na0. 33V2O5 symmetric pseudocapacitor with high performance and high cyclic stability, Chemelectrochem 5 (1) (2018) 101–111.

[54] H. Zhan, et al., Silver frameworks based on self-sintering silver micro-flakes and its application in low temperature curing conductive pastes, J. Mater. Sci. Mater. Electron. 30 (2019) 21343–21354.

[55] I. Mir, D. Kumar, Recent advances in isotropic conductive adhesives for electronics packaging applications, Int. J. Adhesion Adhes. 28 (7) (2008) 362–371.

[56] Y. Li, C. Wong, Recent advances of conductive adhesives as a lead-free alternative in electronic packaging: materials, processing, reliability and applications, Mater. Sci. Eng. R Rep. 51 (1–3) (2006) 1–35.

[57] D. Chen, L. Zhao, H. Diao, W. Zhang, G. Wang, W. Wang, Choice of the low-temperature sintering Ag paste for a-Si:H/c-Si heterojunction solar cell based on characterizing the electrical performance, J. Alloys Compd. 618 (2015/01/05/2015) 357–365, https://doi.org/10.1016/j.jallcom.2014.08.175.

[58] W. Songping, Preparation of micron size flake silver powders for conductive thick films, J. Mater. Sci. Mater. Electron. 18 (2007) 447–452.

[59] M. Ashby, S. Bahk, J. Bevk, D. Turnbull, The influence of a dispersion of particles on the sintering of metal powders and wires, Prog. Mater. Sci. 25 (1) (1980) 1–34.

[60] J. Natsuki, T. Natsuki, Y. Hashimoto, A review of silver nanoparticles: synthesis methods, properties and applications, Int. J. Mater. Sci. Appl. 4 (5) (2015) 325–332.

[61] A. Syafiuddin, Salmiati, M.R. Salim, A. Beng Hong Kueh, T. Hadibarata, H. Nur, A review of silver nanoparticles: research trends, global consumption, synthesis, properties, and future challenges, J. Chin. Chem. Soc. 64 (7) (2017) 732–756.

[62] S. Chen, Y.-H. Mei, M. Wang, X. Li, G.-Q. Lu, Large-area bonding by sintering of a resin-free nanosilver paste at ultralow temperature of 180 C, IEEE Trans. Compon. Packag. Manuf. Technol. 12 (4) (2022) 707–710.

[63] C. Liu, Q. Fu, J. Zou, Y. Huang, X. Zeng, B. Cheng, Effects of polyester resin molecular weight on the performance of low temperature curing silver pastes, J. Mater. Sci. Mater. Electron. 27 (2016) 6511–6516.

[64] Z. Xu, X. Liu, J. Li, R. Sun, L. Liu, Low-temperature sintering of Ag composite pastes with different metal organic decomposition additions, Materials 16 (6) (2023-03-14 2023) 2340, https://doi.org/10.3390/ma16062340.

[65] D. Chen, L. Zhao, H. Diao, W. Zhang, G. Wang, W. Wang, Low-temperature sintering properties of the screen-printed silver paste for a-Si: H/c-Si heterojunction solar cells, J. Mater. Sci. Mater. Electron. 25 (2014) 2657–2664.

[66] C.-A. Lu, P. Lin, H.-C. Lin, S.-F. Wang, Effects of metallo-organic decomposition agents on thermal decomposition and electrical conductivity of low-temperature-curing silver paste, Jpn. J. Appl. Phys. 45 (9R) (2006) 6987.

[67] Y. Hu, et al., Effects of organic additives on the microstructural, rheological and electrical properties of silver paste for LTCC applications, J. Mater. Sci. Mater. Electron. 32 (11) (2021) 14368–14384.

[68] J. Jiu, et al., Die-attaching silver paste based on a novel solvent for high-power semiconductor devices, J. Mater. Sci. 51 (2016) 3422–3430.

[69] H. Zhang, W. Li, Y. Gao, H. Zhang, J. Jiu, K. Suganuma, Enhancing low-temperature and pressureless sintering of micron silver paste based on an ether-type solvent, J. Electron. Mater. 46 (2017) 5201–5208.

[70] I. Kim, S. Chun, Effects of solvent type on low-temperature sintering of silver oxide paste to form electrically conductive silver film, J. Electron. Mater. 40 (2011) 1977–1983.

[71] O. Dagdag, et al., Epoxy resins and their zinc composites as novel anti-corrosive materials for copper in 3% sodium chloride solution: experimental and computational studies, J. Mol. Liq. 315 (2020) 113757.

[72] H. Sembokuya, Y. Negishi, M. Kubouchi, K. Tsuda, Corrosion behavior of epoxy resin cured with different amount of hardener in corrosive solutions, J. Soc. Mater. Sci. 52 (9) (2003) 230–234. Japan.

[73] C. Verma, et al., Epoxy resins as anticorrosive polymeric materials: a review, React. Funct. Polym. 156 (2020/11/01/2020) 104741, https://doi.org/10.1016/j.reactfunctpolym.2020.104741.

[74] O. Dagdag, et al., Cyclotriphosphazene based dendrimeric epoxy resin as an anti-corrosive material for copper in 3% NaCl: experimental and computational demonstrations, J. Mol. Liq. 308 (2020) 113020.

[75] X. Jin, J. Lu, P. Liu, H. Tong, The electrochemical formation and reduction of a thick AgCl deposition layer on a silver substrate, J. Electroanal. Chem. 542 (2003/01/30/2003) 85–96, https://doi.org/10.1016/S0022-0728(02)01474-2.

[76] W.M. Schuette, W.E. Buhro, Silver chloride as a heterogeneous nucleant for the growth of silver nanowires, ACS Nano 7 (5) (2013) 3844–3853.

[77] S.-F. Chen, H. Zhang, Aggregation kinetics of nanosilver in different water conditions, Adv. Nat. Sci. Nanosci. Nanotechnol. 3 (3) (2012) 035006.

[78] X. Li, J.J. Lenhart, H.W. Walker, Dissolution-accompanied aggregation kinetics of silver nanoparticles, Langmuir 26 (22) (2010) 16690–16698.

[79] X. Li, J.J. Lenhart, H.W. Walker, Aggregation kinetics and dissolution of coated silver nanoparticles, Langmuir 28 (2) (2012) 1095–1104.

[80] K.A. Huynh, K.L. Chen, Aggregation kinetics of citrate and polyvinylpyrrolidone coated silver nanoparticles in monovalent and divalent electrolyte solutions, Environ. Sci. Technol. 45 (13) (2011) 5564–5571.

[81] S. Garg, H. Rong, C.J. Miller, T.D. Waite, Oxidative dissolution of silver nanoparticles by chlorine: implications to silver nanoparticle fate and toxicity, Environ. Sci. Technol. 50 (7) (2016) 3890–3896.

[82] J. Yang, Q. Zhang, J.Y. Lee, H.-P. Too, Dissolution–recrystallization mechanism for the conversion of silver nanospheres to triangular nanoplates, J. Colloid Interface Sci. 308 (1) (2007/04/01/2007) 157–161, https://doi.org/10.1016/j.jcis.2006.12.081.

[83] B. Wiley, T. Herricks, Y. Sun, Y. Xia, Polyol synthesis of silver nanoparticles: use of chloride and oxygen to promote the formation of single-crystal, truncated cubes and tetrahedrons, Nano Lett. 4 (9) (2004) 1733–1739.

[84] A. Henglein, T. Linnert, P. Mulvaney, Reduction of Ag+ in aqueous polyanion solution: some properties and reactions of long-lived oligomeric silver clusters and metallic silver particles, Ber. Bunsen Ges. Phys. Chem. 94 (12) (1990) 1449–1457.

[85] A. Fargašová, R. Prucek, V. Ranc, A. Panáček, L. Kvítek, R. Zbořil, Influence of various chloride ion concentrations on silver nanoparticle transformations and effectiveness in surface enhanced Raman scattering for different excitation wavelengths, RSC Adv. 5 (13) (2015-01-01 2015) 9737–9744, https://doi.org/10.1039/c4ra13881c.